NONLOCAL MICROPLANE CONCRETE MODEL WITH RATE EFFECT AND LOAD CYCLES. II: APPLICATION AND VERIFICATION

By Toshiaki Hasegawa[1] and Zdeněk P. Bažant,[2] Fellow, ASCE

ABSTRACT: This second part of the study deals with experimental verification of an improved and generalized nonlocal microplane model whose general formulation was given in the first part. First the stress-strain relations for a material point are simulated with a local version of the model, and then the representation of some basic tests is studied in finite-element analyses with the nonlocal calculation.

INTRODUCTION

Part I of this study (Hasegawa and Bažant 1993) presented various improvements and extensions of the microplane model for concrete. The purpose of this second part is to demonstrate the capability to simulate the pertinent test data. All definitions and notations from part I are retained.

The postpeak response of specimens with strain-softening damage or fracture must be suspected to involve strain localization and size effect, and cannot be interpreted as if the specimens were in a uniform state. This means that the numerical results we get with one finite element using a local version of the microplane model are insufficient to compare with the experimental results and verify the model. Subdivision of the specimens into many finite elements is needed to do that. Nevertheless, as the first check of the constitutive model, the point response, calculated with one finite element, needs to be explored and understood.

SIMULATION OF MACROSCOPIC STRESS-STRAIN RELATION FOR MATERIAL POINT

Except for the elastic constants, Young's modulus E and Poisson's ratio ν, each microplane in the present model is characterized by three groups of material parameters: The first group involves the material parameters for the virgin stress-strain curves, i.e. σ_{NT}^0, ζ_{NT}, γ_{NT}, and p_{NT} for (31) of part I; σ_{NC}^0, ζ_{NC}, γ_{NC}, and p_{NC} for (32) of part I; σ_T^0, ζ_T, γ_T, p_T, and μ for (37) and (38) of part I; C_N^f, ε_a, ε_b, p_H, and q_H for (33) and (34) of part I; and ε_{LD}^t, ε_{LD}^v, and m for (27) of part I. The second group involves the material parameters for unloading-reloading, i.e. α_{NT} and α_{NC} for (35) of part I; α_T for (39) of part I; and $U_{\max}$, $U_{\min}$, $R_{\max}$, and $R_{\min}$ for (44) of part I. The third group involves the relaxation times ρ in (12) of part I. For $U_{\max}$, $U_{\min}$, $R_{\max}$, $R_{\min}$ and ρ we have separate values for normal tension, normal compression, and shear. Altogether, there are 39 material parameters. However, according to the data-fitting experience it appears that one does not have to specify the individual values for α_{NT}, α_{NC}, and α_T as well as those for $U_{\max}$, $U_{\min}$, $R_{\max}$, and $R_{\min}$ in normal tension, normal compression, and shear. Also, it appears that one can set $U_{\max} = R_{\max}$ and $U_{\min} = R_{\min}$ because, if $U_{\max} \neq R_{\max}$ or $U_{\min} \neq R_{\min}$, the shapes of the hysteresis loops are sometimes unacceptable. It means that we can reduce the number of independent microplane material parameters to 27.

By fitting cyclic uniaxial compressive and tensile test data for concrete, the following values characterizing the unloading-reloading rule were found to work:

$$U_{\max} = R_{\max} = 2.0 \quad \ldots\ldots (1a)$$

$$U_{\min} = R_{\min} = 0.5 \quad \ldots\ldots (1b)$$

$$\alpha_{NT} = \alpha_{NC} = \alpha_T = 0.2 \quad \ldots\ldots (1c)$$

In the case of normal hydrostatic response, the hysteresis loops of a microplane should be very narrow because little damage is done to the material; in the case of normal compressive softening response, the hysteresis loops should be wide. However, no hysteresis is assumed for normal compressions including softening, for the sake of simplicity.

Since under hydrostatic condition there is no shear on the microplanes, the material parameters C_N^f, ε_a, ε_b, p_H, and q_H for the hydrostatic curve [(33) of part I] can be determined independently of all the others, simply by direct fitting of the experimental data for hydrostatic compression of concrete. Such a fitting of the test data of Green and Swanson (1973) is shown in Fig. 1(*a*), and the material parameters identified are $C_N^f = C_N^0$; $\varepsilon_a = -0.0013$; $\varepsilon_b = -0.17$; and $p_H = q_H = 1.0$. Although there exist only limited hydrostatic compression test data for concrete, they show that we may assume the asymptotic final modulus (slope) for the hydrostatic curve to be the same as the initial modulus, i.e., $C_N^f = C_N^0$. For most individual data sets of concrete, the hydrostatic response curve has not been measured, and therefore the parameters determined for the test data of Green and Swanson are used in all the present calculations.

Since in most static loading tests of concrete only one strain rate has been used, it is impossible to identify the microplane material parameters governing the rate effect, i.e. relaxation times ρ. Therefore, in the following

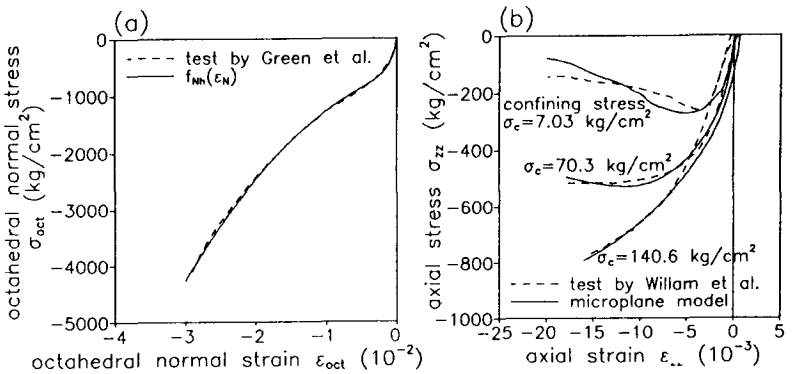

FIG. 1. (*a*) Comparison with Hydrostatic Compression Test by Green and Swanson (1973); (*b*) Comparison with Triaxial Compressive Tests by Willam et al. (1986)

[1]Struct. Res. Engr., Shimizu Corp., 3-4-17 Etchujima, Koto-ku, Tokyo 135, Japan.
[2]Walter P. Murphy Prof. of Civ. Engrg., Northwestern Univ., 2145 Sheridan Rd., Evanston, IL 60208-3109.

Note. Discussion open until January 1, 1994. Separate discussions should be submitted for the individual papers in this symposium. To extend the closing date one month, a written request must be filed with the ASCE Manager of Journals. The manuscript for this paper was submitted for review and possible publication on September 23, 1991. This paper is part of the ***Journal of Materials in Civil Engineering***, Vol. 5, No. 3, August, 1993. ©ASCE, ISSN 0899-1561/93/0003-0394/$1.00 + $.15 per page. Paper No. 2742.

calculations for the static loading tests we have to eliminate the strain rate effect by specifying infinite values of the relaxation times ρ^{ν}. According to the numerical simulations of one microplane response with different relaxation times and strain rates, the values of the relaxation times ρ^{ν} seem to be functions of the strain rate and the peak stress value for the monotonic curve. In the case of calculations for the typical static strain rates used in experiments, $\dot{\epsilon} = 10^{-6}$–10^{-5}/s, it seems possible to consider the relaxation times $\rho^{\infty}_{NT} = \rho^{\infty}_{T} = 10^5$ s and $\rho^{\infty}_{NC} = 10^6$ or 10^7 s as infinite.

First some comparisons with the previous microplane model should be mentioned. In the previous microplane model (Bažant and Prat 1988; Bažant and Ožbolt 1990; Ožbolt and Bažant 1991; Carol et al. 1992), a good description of the response in compression softening was achieved by splitting the resolved normal microstrain component into volumetric and deviatoric components, which meant that the microplane response was indirectly affected by the lateral strain. This split made it possible to describe materials with arbitrary Poisson ratios ν, within the range $-1 \leq \nu \leq 0.5$, which is an advantage over the present model (in which an arbitrary Poisson's ratio cannot be obtained). However, the fact that the lateral strain has only an indirect effect, as a part of the volumetric strain, may be a disadvantage, detracting from conceptual clarity. Whereas the differences in the capabilities of these two related but different approaches remain to be explored deeper, we adhere here to the direct use of lateral strain, with no volumetric-deviatoric split of the normal strain.

Fig. 2 shows an example of response for the uniaxial compressive test, in which the formulations for the volumetric, deviatoric and shear components on all microplanes are combined. The material parameter values are as follows: (1) For volumetric tension $\sigma^0_{VT} = 2.45$ MPa, $\zeta_{VT} = 0.9$, γ_{VT}

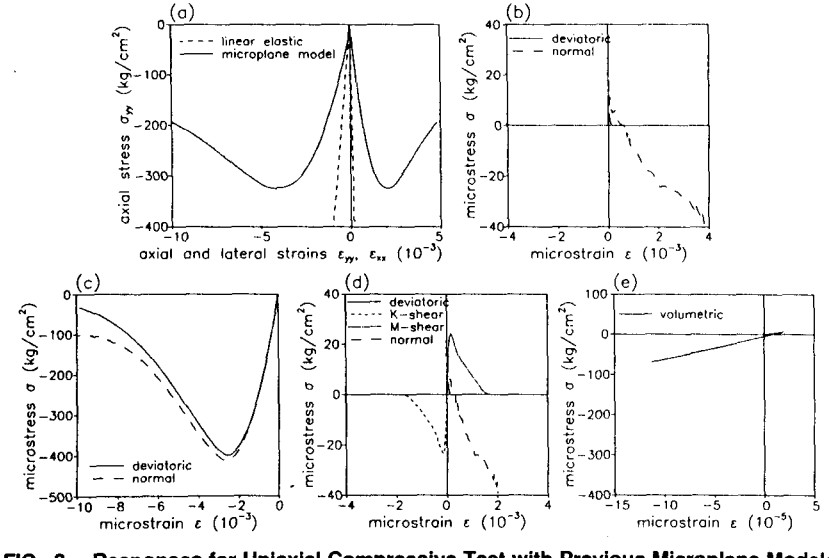

FIG. 2. Responses for Uniaxial Compressive Test with Previous Microplane Model: (a) Macroscopic Stress-Strain Response; (b) Microstress-Strain Responses at Integration Point 1; (c) Microstress-Strain Responses at Integration Point 2; (d) Microstress-Strain Responses at Integration Point 18; (e) Volumetric Response

$= 3.0$, $p_{VT} = 2.0$, $\rho_{VT} = 10^5$ s, and $\eta_0 = C^0_D/C^0_V = 1.0$; (2) for deviatoric tension $\sigma^0_{DT} = 0.49$ MPa, $\zeta_{DT} = 0.9$, $\gamma_{DT} = 3.0$, $p_{DT} = 2.0$, and $\rho_{DT} = 10^5$ s; (3) for deviatoric compression $\sigma^0_{DC} = -39.23$ MPa, $\zeta_{DC} = 0.5$, $\gamma_{DC} = 1.5$, $p_{DC} = 1.5$, and $\rho_{DC} = 10^6$ s; and (4) for shear $\sigma^0_T = 1.47$ MPa, $\zeta_T = 0.5$, $\gamma_T = 1.5$, $p_T = 1.5$, $\mu = 1.0$, and $\rho_T = 10^5$ s. The numerical integration over the spherical surface of microplane orientations was done using Bažant and Oh's (1986) formula with 21 integration points per hemisphere [Fig. 1(*d*) of part I]. (The uniaxial compression direction coincided with the direction of the unit normal vector at integration point 2.) Fig. 2(*a*) shows the macroscopic stress-strain curve and Figs. 2(*b–d*) show for integration points 1, 2, and 18 (the deviatoric response and the shear responses of the K and M directions) and the total normal response as a sum of the deviatoric and volumetric components. Fig. 2(*e*) shows the volumetric response. The microplane at integration point 2 affects mainly the axial response, while the microplane at integration point 1 affects mainly the Poisson effect and volume dilatancy. The microplane at integration point 18 has a high intensity of shear strain, while integration points 1 and 2 have no shear strains.

Since a few existing hydrostatic tension tests show that the macroscopic hydrostatic tensile strength of concrete is approximately equal to the macroscopic uniaxial tensile strength f_t, we have to choose the volumetric peak tensile stress value σ^0_{VT} equal to the macroscopic uniaxial tensile strength f_t. However, the macroscopic uniaxial tensile peak stress calculated with the microplane volumetric-deviatoric-shear formulation is then higher than the sum of the deviatoric peak tensile stress value σ^0_{DT} and the volumetric peak tensile stress σ^0_{VT}. This means that we should set σ^0_{VT} as close to f_t as possible and σ^0_{DT} as small as possible because a reasonable triaxial failure envelope in the tensile region could not otherwise be obtained. Therefore, in calculating Fig. 2, a small value of σ^0_{DT} ($=0.49$ MPa) and a larger value of σ^0_{VT} ($=2.45$ MPa) were chosen. But this goes against the assumption of the previous model that the stress-strain curves for volumetric tension and deviatoric tension are the same. The use of a small value of σ^0_{DT} causes the damage on each microplane to occur earlier, especially on the microplanes that resist lateral dilation in the case of uniaxial compression; this causes a deviation from purely elastic behavior at lower stress level. This is the reason why the response seen in Fig. 2(*a*) is far away from purely elastic behavior [dotted straight lines in Fig. 2(*a*)] already at the beginning of stressing. To avoid this, a material constant η_0 ($= C^0_D/C^0_V$), representing the ratio between the initial deviatoric and volumetric moduli, was changed for these calculations, but no better result had been available.

One interesting result is the volumetric response, which shows a volumetric dilatation to occur at the beginning and a volumetric compaction after that, as seen in Fig. 2(*e*). It is an opposite trend to that in the study of Bažant and Prat (1988), in which reasonable results were obtained showing the initial volumetric compaction and subsequent volumetric dilatation. The reason was the assumption that $\sigma^0_{DT} = \sigma^0_{VT}$ and that the stress-strain curves for deviatoric and volumetric tensions are the same. However, the assumption $\sigma^0_{DT} = \sigma^0_{VT}$ appears questionable from the viewpoint of the macroscopic triaxial strength envelope, as already mentioned.

To compare the present normal-shear formulation with the previous volumetric-deviatoric-shear formulation, Fig. 3 presents the numerical results for uniaxial compression using the present microplane model, and Table 1 gives the corresponding material parameters. Fig. 3(*a*) shows the calculated

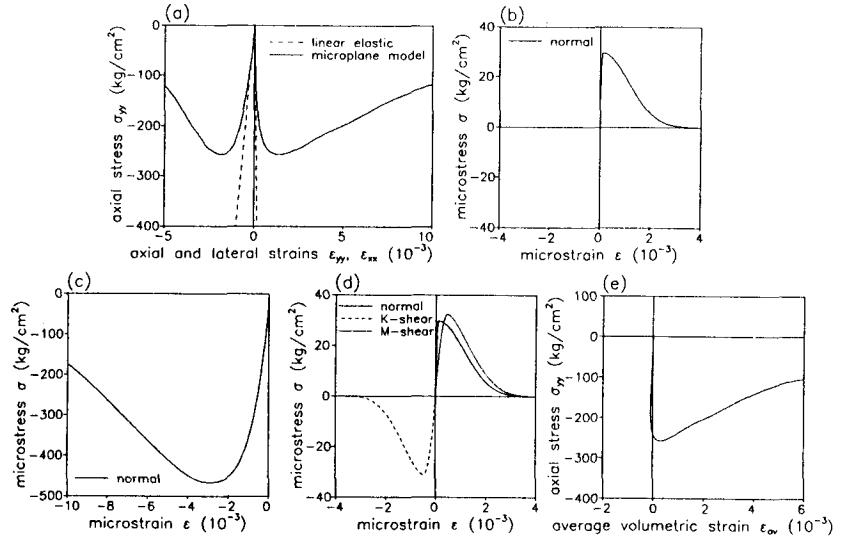

FIG. 3. Responses for Uniaxial Compressive Test with Present Microplane Model: (*a*) Macroscopic Stress-Strain Response; (*b*) Microstress-Strain Response at Integration Point 1; (c) Microstress-Strain Response at Integration Point 2; (*d*) Microstress-Strain Responses at Integration Point 18; (*e*) Macroscopic Volumetric Response

macroscopic stress-strain response. Figs. 3(*b–d*) show the normal, *K*-shear, and *M*-shear responses for integration points 1, 2, and 18 (the same as in Fig. 2). Fig. 3(*e*) shows the resulting relation between the macroscopic axial stress σ_{yy} and the macroscopic average volumetric strain ε_{av} ($\varepsilon_{av} = \varepsilon_{ii}/3$). Compared with the responses on the microplanes in the previous formulation (Fig. 2), the responses for the present formulation appear quite reasonable. The response at integraton point 1 is a progressive tensile softening behavior, which reflects axial tensile cracking in the uniaxial compressive specimen [Fig. 3(*b*)]. In the calculation, the macroscopic compressive peak is obtained when the shear responses on some microplanes (integration points 4, 5, 6, 7, 10, 11, 12, and 13) go into the softening regimes after the normal responses on the same microplanes go into softening. This appears to be a consistent picture of the micromechanism of uniaxial compressive failure, in which the uniaxial compressive specimen is weakened by axial splitting cracks. The main difference from the results with the previous formulation is the relation between the macroscopic axial stress σ_{yy} and the macroscopic average volumetric strain ε_{av}, shown in Fig. 3(*e*). In contrast to the previous formulation [Fig. 2(*e*)], the present volumetric response is consistent with the experimental fact that the volumetric compaction precedes the volumetric dilatation due to axial tensile cracking. The turning point from volumetric compaction to dilatation, which is sometimes called the critical point and occurs in experiments usually at 75–90% of uniaxial compressive strength f'_c, is here obtained at 78% of f'_c.

Fig. 1(*b*) shows the fits of the triaxial compressive test data for concrete by Willam et al. (1986), and Table 1 gives the material parameters used. These tests, which were carried out at three different confining stress levels

TABLE 1. Optimum Values of Material Parameters

Material Parameter (1)	(2)	(3)	Fig. 3 (4)	Willam et al. (1986) (5)	van Mier (1984) (6)	Karsan and Jirsa (1969) (7)	Reinhardt and Cornelissen (1984) (8)	Dilger et al. (1984) (9)
Normal tension	σ^0_{NT}	kg/cm^2	30.0	26.0	65.0	26.0	21.0	45.0
	ζ_{NT}	—	0.5	0.5	0.5	0.5	0.6	0.5
	γ_{NT}	—	15.0	5.0	5.0	10.0	5.0	10.0
	p_{NT}	—	2.0	1.5	1.5	1.5	1.5	1.5
	ρ_{NT}	sec	10^5	10^5	10^5	10^5	10^5	3.0×10^2
Normal compression (softening)	σ^0_{NC}	kg/cm^2	−400.0	−340.0	−640.0	−300.0	−600.0	−350.0
	ζ_{NC}	—	0.2	0.4	0.3	0.4	0.4	0.4
	γ_{NC}	—	2.0	2.0	2.0	2.0	2.0	2.0
	p_{NC}	—	1.5	1.5	1.5	1.5	1.5	1.5
	ρ_{NC}	sec	10^6	10^7	10^7	10^7	10^7	3.0×10^3
Shear	σ^0_T	kg/cm^2	15.0	15.0	50.0	10.0	10.0	15.0
	ζ_T	—	0.5	0.6	0.8	0.8	0.8	0.8
	γ_T	—	3.0	2.0	1.5	6.0	1.5	4.0
	p_T	—	1.5	1.5	1.5	1.5	1.5	1.5
	μ	—	0.5	1.0	0.5	0.5	0.5	0.5
	ρ_T	sec	10^5	10^5	10^5	10^5	10^5	3.0×10^2
Lateral strain effect	ε^1_{LD}	—	0.002	0.01	0.01	0.01	0.01	0.01
	ε^2_{LD}	—	0.002	0.01	0.01	0.01	0.01	0.01
	m	—	1.0	1.0	1.0	1.0	1.0	1.0
Experimental data	f'_c	kg/cm^2	—	225.0	431.0	193.0[a]	463.0[b]	237.0
	f_t	kg/cm^2	—	26.0	28.0[c]	—	23.0[a]	—

[a]Peak stress in test.
[b]Cubic specimen.
[c]Concrete of a different batch with the same mix proportion.

(σ_c = 0.69, 6.90, and 13.79 MPa), show the confinement effect, i.e., the transition from the softening response at σ_c = 0.69 MPa to the plastic hardening response at σ_c = 13.79 MPa. The feature that enables the present microplane model to describe the confinement effect is the dependence of the normal response on the lateral strains and also the dependence of the peak shear microstress value on the resolved normal macroscopic stress tensor. The former dependence is included in parameter ε^l_{LD}, ε^p_{LD}, and m, and the latter dependence is included in parameter μ. The fits in Fig. 1(b) are good, which means that the present normal-shear formulation with lateral strain dependence and the resolved normal macroscopic stress tensor dependence is valid without resorting to the volumetric-deviatoric subdivision of the normal microplane strain. The other tests simulated in this study include no data with different confining stress levels, therefore in the latter calculations the parameters fitted to the test data of Willam et al. (1986), ε^l_{LD} = 0.01, ε^p_{LD} = 0.01, and m = 1.0, are used for the sake of simplicity.

Figs. 4 and 5 show the fits of the cyclic uniaxial compressive tests of concretes by van Mier (1984) and by Karsan et al. (1960), and Table 1 lists the corresponding material parameters. As before, Fig. 4(b–d) and Fig. 5(b–d) show the normal, K-shear and M-shear responses at integration points 1, 2, and 18. From these results we can see a good capability of the present model in describing macroscopic cyclic behaviors including degradation of the unloading-reloading stiffness and the shapes of the hysteresis loop, particularly the change of the loop width. The integration points 1 correspond to the lateral directions for uniaxial compression and their responses simulate axial splitting cracks. Note that even though the microplane

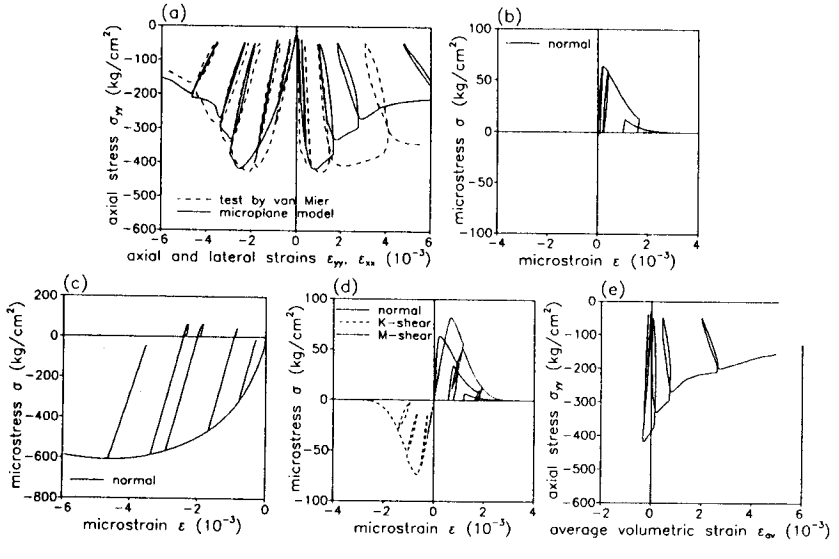

FIG. 4. Comparison with Cyclic Uniaxial Compressive Test by van Mier (1984): (*a*) Macroscopic Stress-Strain Response; (*b*) Microstress-Strain Response at Integration Point 1; (*c*) Microstress-Strain Response at Integration Point 2; (*d*) Microstress-Strain Responses at Integration Point 18; (*e*) Macroscopic Volumetric Response

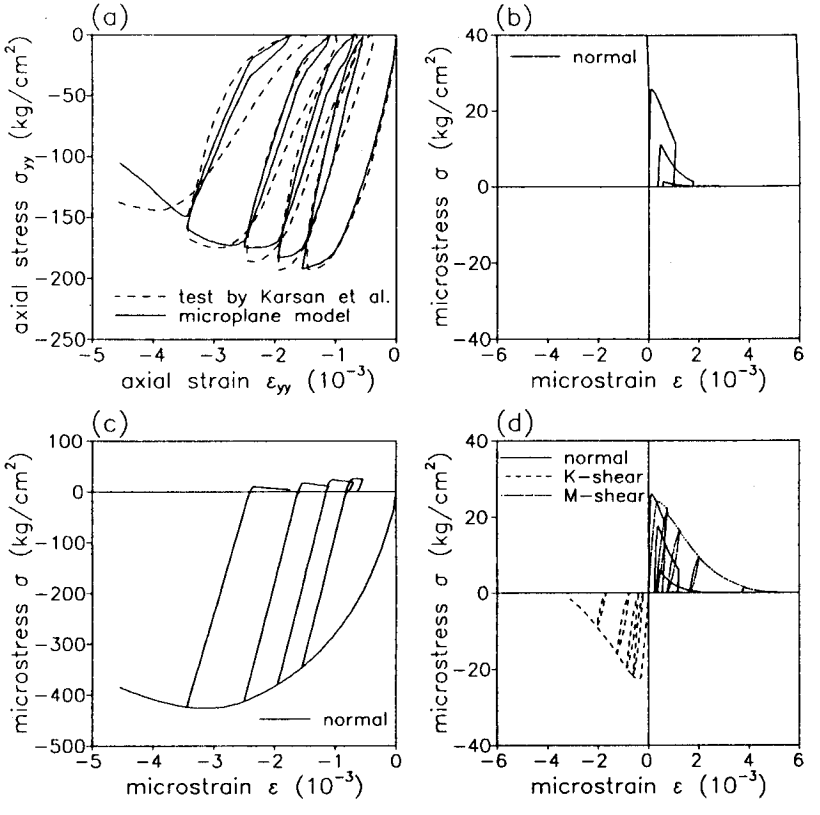

FIG. 5. Comparison with Cyclic Uniaxial Compressive Test by Karsan and Jirsa (1969): (*a*) Macroscopic Stress-Strain Response; (*b*) Microstress-Strain Response at Integration Point 1; (*c*) Microstress-Strain Response at Integration Point 2; (*d*) Microstress-Strain Responses at Integration Point 18

responses at integration points 2 corresponding to the direction of uniaxial compression have no hysteresis loops, the macroscopic responses for the same strain values as those for integration points 2 do have hysteresis loops. It means that the source of macroscopic hysteresis lies mainly in the hysteresis loops for normal tensile softening and shear softening on the microplanes.

Fig. 6 compares the calculated results with Reinhardt's (1984) cyclic uniaxial tensile tests, in which tapered cylindrical specimens were used, with saw-cut notches inducing a crack at mid length. The displacement across the notch was measured over the base length of 25 mm. The average strain over the base length was compared to the present calculations. The identified material parameters are again listed in Table 1. The calculated results agree well with these test data, especially the postpeak stiffness degradation and the linear compressive behavior.

Fig. 7(a) compares the uniaxial compressive tests data (Dilger et al. 1984) for different strain rates (-3.3×10^{-5} to -2.0×10^{-1} s^{-1}) with the calculated results using the relaxation times ρ given, along with other material parameters, in Table 1. The ρ-values have totally different orders of

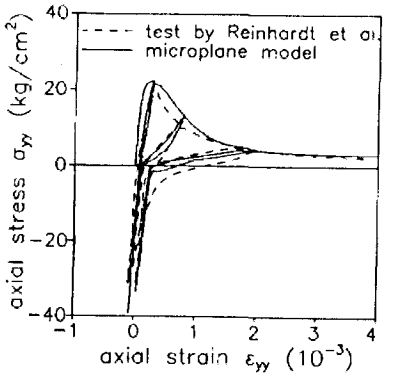

FIG. 6. Comparison with Cyclic Uniaxial Tensile Test by Reinhardt and Cornelissen (1984)

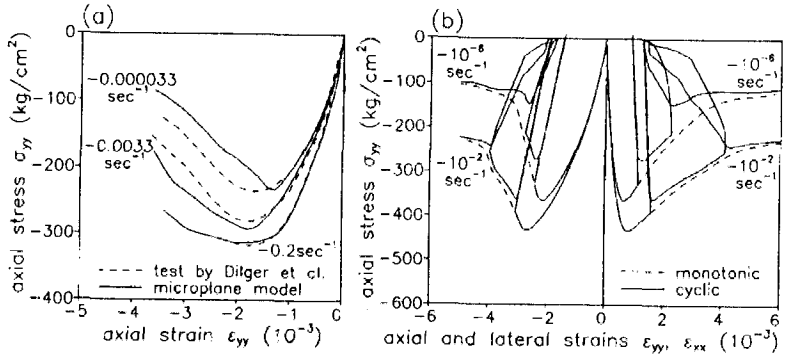

FIG. 7. (*a*) Comparison with Uniaxial Compressive Tests for Different Strain Rates by Dilger et al. (1984); (*b*) Prediction of Cyclic Responses with Different Strain Rates, Using Material Parameters Corresponding to van Mier's (1984) Test Data

magnitude than in the previous static calculations because the strains range from static to dynamic (impact). In the calculation, different values of Young's modulus E are used for different strain rates, since, otherwise, the initial prepeak response would deviate from the test results (for $\dot{\varepsilon} = 3.3 \times 10^{-5}$, -3.3×10^{-3}, and -2.0×10^{-1} s^{-1}: $E = 3.24 \times 10^4$, 3.43×10^4, and 4.22×10^4 MPa). (This could be avoided by introducing strain-rate dependence in the elastoplastic-fracturing element of the generalized Maxwell model for each microplane, but this would further complicate the model.) Although the fits are not poor, more extensive comparisons are desirable.

There are only few experimental data on the strain rate effect, especially for cyclic loading. We consider van Mier's (1984) cyclic uniaxial compression data. The relaxation times are assumed as $\rho_{NT} = \rho_T = 1.0 \times 10^4$ s; $\rho_{NC} = 1.0 \times 10^5$ s; and the monotonic and cyclic loading calculations are done for two strain rates, $\dot{\varepsilon} = -1.0 \times 10^{-6}$ and -1.0×10^{-2} s^{-1}. In each, the unloading-reloading cycles start at two postpeak stress values $0.9\sigma_{peak}$ and $0.6\sigma_{peak}$, where σ_{peak} = peak stress for monotonic loading. The results are shown in Fig. 7(*b*). The decreases of the load capacities due to cycling,

which are defined as stress differences between the monotonic and cyclic curves, get smaller as the strain rate gets larger.

One advantage of the present microplane model is that each material parameter has a clear, easily understandable, mechanical meaning. For example, σ^0 are the peak microstresses for each component, γ represent the ductilities in the postpeak range, and ζ represent the strains at peak stress, characterizing the degree of nonlinearity in the prepeak response. The values in Table 1 illuminate the choice of material parameters for the microplane model; σ^0_{NT} and σ^0_T appear to be related not only to f_t but also to f'_c; σ^0_{NT} can control the stress level for the critical point of uniaxial compressive stress-strain curve; σ^0_{NC} does not have a strong correlation with f'_c, but we might consider it to be larger than f'_c. From numerical experience, $\sigma^0_{NT} = (1.0\text{–}2.0)f_t$, $\sigma^0_{NC} \cong -1.5f'_c$, and $\sigma^0_T = (0.5\text{–}1.5)f_t$. The values of ζ_{NT} and ζ_{NC} do not have large effects on the macroscopic behavior; however, ζ_{NC} must be chosen so that the normal compressive softening curve touches inside of the normal hydrostatic curve. On the other hand, the value of ζ_T can change the macroscopic peak stress and the ductilities in uniaxial compressive test. From numerical experience, $\zeta_{NT} = 0.4\text{–}0.6$, $\zeta_{NC} = 0.3\text{–}0.5$, and $\zeta_T = 0.4\text{–}0.8$. There seems to be a tendency of large γ_{NT} and γ_T values to yield higher peak stresses and ductilities in the macroscopic responses. The value γ_{NC} seems to have a small effect on the macroscopic uniaxial compressive and tensile behaviors. The values p_{NT}, p_{NC}, and p_T change the postpeak softening curves only slightly (the ductilities depend mainly on γ). From such experience, $p_{NT} = p_{NC} = p_T = 1.5$. The larger the frictional coefficient μ of the shear component, the more prominent the confinement effect in triaxial tests. However, if μ becomes too large, the volumetric dilatation near the uniaxial peak stress disappears. From experience, $\mu = 0.5\text{–}1.0$.

With the foregoing parameters fixed as indicated, 10 material parameters remain to be identified by fitting individual monotonic test data (namely σ^0_{NT}, σ^0_{NC}, σ^0_T, ζ_{NT}, ζ_{NC}, ζ_T, γ_{NT}, γ_{NC}, γ_T, and μ) provided that the parameters of the hydrostatic curve and the lateral strain effect have already been fixed.

Note that all the test data used were obtained at fixed principal stress rotations. We cannot guarantee that if their directions rotate, some modifications of the model might not be needed. In principle, however, the microplane model should apply to rotating principal stress directons as well.

As important feature to note is that the test data were fitted under the assumption of a uniform strain state. Obviously this is generally not true for postpeak softening. Localizations likely occurred, and consequently the postpeak response obtained with the present model applies only to specimen sizes approximately the same as those tested. But calculations in the postpeak softening range can be made using some form of a localization limiter, for which the nonlocal theory is adopted here.

NUMERICAL STUDIES WITH NONLOCAL MICROPLANE MODEL

The present microplane model has been combined with the nonlocal theory, and the microplane finite-element program has been generalized for the nonlocal behavior. This makes it possible to model the size effects, which were investigated in the previous studies of the nonlocal smeared-cracking model and nonlocal microplane model (Bažant and Lin 1988; Bažant and Ožbolt 1990). Those studies dealt with tensile cracking and fracture. The present microplane model is more general and has been partly verified

for more general stress conditions. We are interested in applying it to nontensile failures. We explore a set of experiments available in the literature, those of van Mier (1984), dealing with uniaxial compressive failures of prisms of the same square section (100 × 100 mm) but different heights (50, 100, and 200 mm). These tests, strictly speaking, do not show what is understood as the size effect, because the specimens were not geometrically similar. Van Mier's tests show that the postpeak descending stress-strain diagram becomes steeper as the specimen height (length) (or the height-to-width ratio, slenderness) is increased.

Fig. 8 shows the three finite-element meshes used. Meshes A, B, and C correspond to van Mier's specimens 15A1-5 (height h = 50 mm), 10B1-3 (h = 100 mm), and 10B2-2 (h = 200 mm): They consist of 25 four-node isoparametric finite elements with 2 × 2 Gaussian integration points. The plane stress condition is assumed. The boundary conditions on the loaded sides are a sliding (frictionless) constraint in the x-direction. The load is introduced by prescribing uniform nodal displacements along the loaded side. The material parameters are the same as those indicated for the simulation of van Mier's cyclic uniaxial compressive test (Table 1). The characteristic length l is assumed to be $l = 3d_a = 3 \times 16$ mm = 48 mm (d_a is maximum aggregate size). The finite-element calculations are done not only with nonlocal averaging, but also without it.

The calculated load-displacement curves are compared to van Mier's data in Fig. 9(a). The load-displacement curves for both local and nonlocal calculations are almost the same in the cases of h = 50 and 100 mm, and they both agree with the experiments well. However, in the case of h = 200 mm, the maximum load value for the local calculation is too small, while the nonlocal calculation predicts the maximum well. Generally, the numerical convergence of the load-step iterations in the local calculations has not been good, although for the nonlocal calculations it has been very good. The reason is spurious strain localization in the case of local calculations; the nonlocal calculations do not have such a problem, as shown later.

Fig. 10 shows the distributions of strain ε_{xx} (lateral strain) at maximum load ($P = P_{max}$) for all the meshes; Fig. 10(a–c) are the nonlocal calculations, and Fig. 10(d–f) are the local calculations (here and in Figs. 11–13).

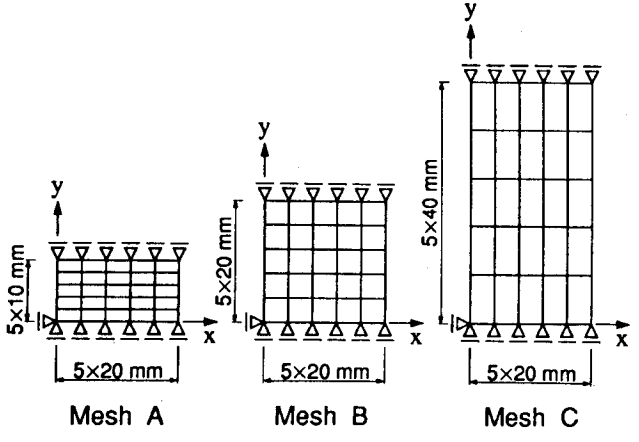

FIG. 8. Finite-Element Meshes for van Mier's (1974) Specimens

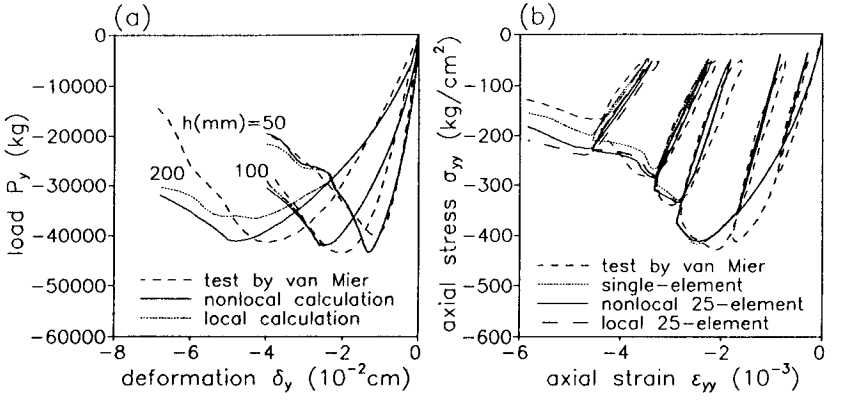

FIG. 9. (*a*) Comparison with van Mier's (1984) Tests on Effect of Height-to-Width Ratio; (*b*) Comparison with Cyclic Uniaxial Compressive Test by van Mier (1984) (Nonlocal 25-Element Calculation, Local 25-Element Calculation and Single Element Calculation)

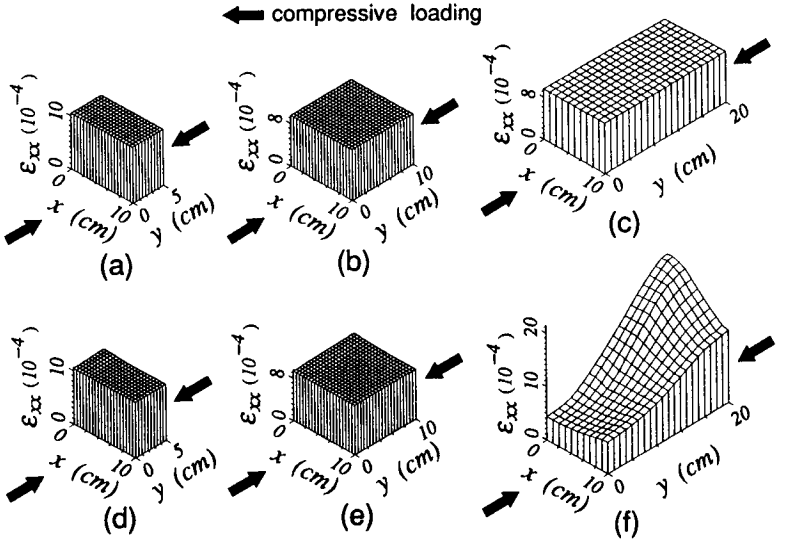

FIG. 10. Calculated Lateral Strain Distributions ε_{xx} at Maximum Load P_{max} for van Mier's (1984) Tests: (*a*)–(*c*) Nonlocal Calculations; (*d*)–(*f*) Local Calculations

There are only small differences between the distributions for nonlocal and local calculations for the heights h = 50 and 100 mm, but for h = 200 mm the strain distributions are very different, the strain field for the local calculation tends to localize. Fig. 11 shows the ε_{xx} distributions at postpeak load $P = 0.7P_{max}$ for all the meshes [the strain scale of Fig. 11(f) is different from the others]. A large strain localization occurs in the local case for h = 200 mm [Fig. 11(f)]; in the nonlocal case there is no pronounced localization, only a gradual strain distribution [Fig. 11(c)]. The localization ob-

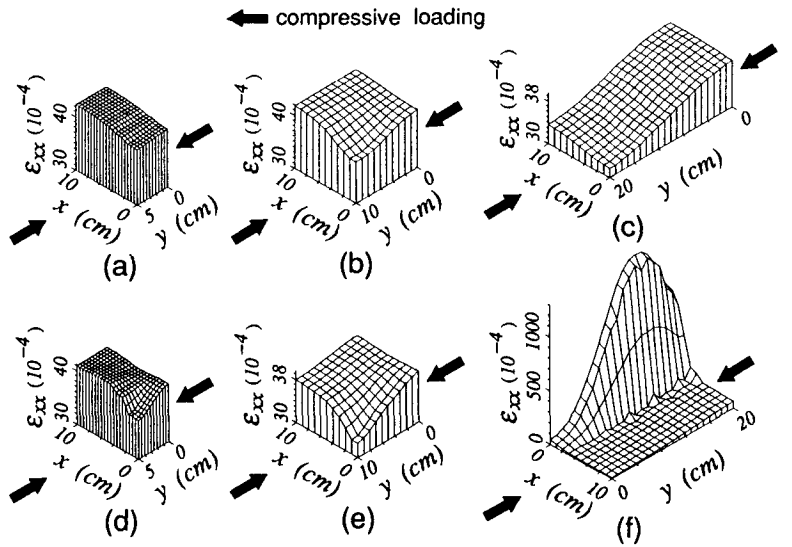

FIG. 11. Calculated Lateral Strain Distributions ε_{xx} at Load on Softening Regime ($P = 0.7P_{max}$) for van Mier's (1984) Tests: (a)–(c) Nonlocal Calculations: (d)–(f) Local Calculations

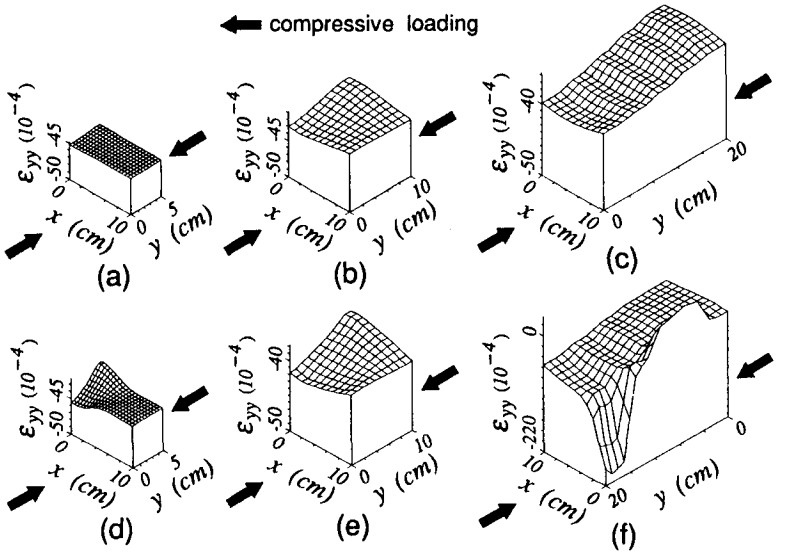

FIG. 12. Calculated Compressive Axial Strain Distributions ε_{yy} at Load on Softening Regime ($P = 0.7P_{max}$) for van Mier's (1984) Tests: (a)–(c) Nonlocal Calculations; (d)–(f) Local Calculations

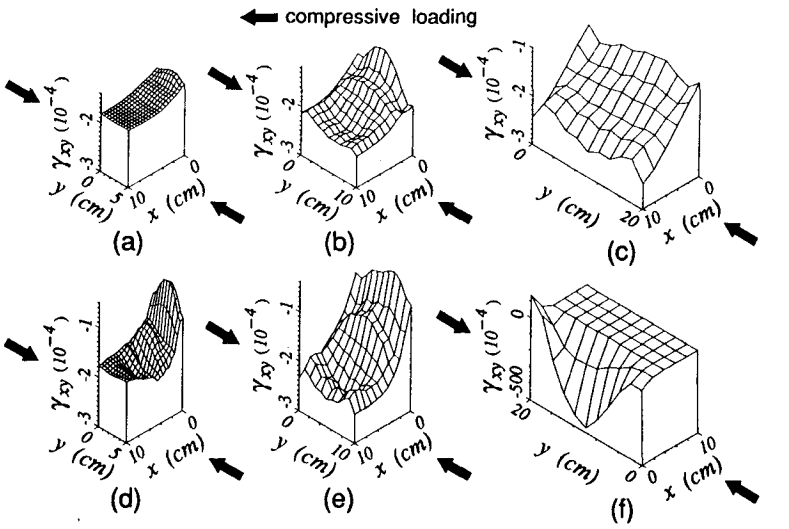

FIG. 13. Calculations Shear Strain Distributions γ_{xy} at Load on Softening Regime ($P = 0.7P_{max}$) for van Mier's (1984) Tests: (a)–(c) Nonlocal Calculations: (d)–(f) Local Calculations

tained in the local case seems to be spurious, due to numerical problems, which is indicated by poor numerical convergence and the fact that localization is seen to occur in only a single element band at $x = 0$ to 2 cm. Comparing the nonlocal and local cases for the heights $h = 50$ and 100 mm, the local case always gives a stronger localization than the nonlocal case.

Fig. 12 shows the distributions of ε_{yy} (compressive axial strain) at postpeak load $P = 0.7P_{max}$ for all the meshes [the strain scale of Fig. 12(*f*) is different from the others]. We can observe the same phenomena as in the case of ε_{xx}. Fig. 13 compares the distributions of shear strain γ_{xy} at postpeak load $P = 0.7P_{max}$, for all the meshes [the strain scale of Fig. 13(*f*) is different from the others]. At the maximum load, there are almost no shear strains in all the cases except the local case of $h = 200$ mm, in which the shear strains are localized. However, in Fig. 13 for the softening response the shear strains in all the cases are relatively large compared to those at the maximum load, especially in the local case for $h = 200$ mm [Fig. 13(*f*)]. The shear strain localization tends to increase with the mesh sizes, and the localization is more pronounced for the local cases.

To summarize the comparisons in Figs. 10–13, the nonlocal calculations always yield numerically stable solutions regardless of the specimen height or the element size; and the local calculations yield spurious localizations and poorer convergence when specimens much larger than l are analyzed. The nonlocal results of course do not represent the actual microstrains but macroscopically smoothed (averaged) strains.

The aforementioned strain distributions reveal differences in the failure mechanisms for different specimen heights. The first stage of damage is characterized by splitting cracks in the direction of compressive axis, as revealed by large values of the calculated lateral strains ε_{xx} in Figs. 10 and 11. After the peak load, the shear strains γ_{xy} increase markedly and tend to localize; prior to the peak load there is almost no shear strain. The shear

localization is more intense when the specimen height is larger. Since the shear localization represents local failure and may lead to buckling of the material strips between the splitting cracks, the load-carrying capacity of the specimens with larger height decreases at an earlier stage of the softening regime than for the specimens with smaller height. According to experimental observations, uniaxial compressive specimens without friction under the loading platens usually do not fail by shear bands but by axial splitting. The final failure probably occurs by snap-through buckling of the material strips between the splitting cracks. These experimental facts are consistent with the present analytical results.

In the present calculations, the finite elements were relatively large compared with the specimen sizes and with the characteristic length l. Thus it might be that the element subdivision might not be sufficiently fine to represent the deformation field, and especially the shear band localization mode. Calculations with finer meshes are desirable.

In this study, the characteristic length l is fixed as $l = 3d_a$, which is the approximation suggested for the crack-band theory (Bažant and Oh 1983). The effect of changing l has not been explored, but the estimate $l = 3d_a$ is certainly a crude guess and the value l would better be identified by fitting of more extensive test data on the effects of both the height-to-width ratio and the specimen size for the same height-to-width ratio. But such comprehensive test data are lacking.

It is interesting to compare the cyclic calculation results using the nonlocal and local microplane models. Van Mier's (1984) cyclic uniaxial compressive test data for the specimen with height $h = 100$ mm were fitted in Fig. 4 with a single finite element, and mesh B (100 × 100 mm) is then used along with the same material parameters given in Table 1. Fig. 9(*b*) shows the calculated stress-strain curves along with the previous result using a single finite element, for comparison (the load-displacement data were converted into average stress-strain data for the total specimen height). The differences between the nonlocal 25-element calculation, the local 25-element calculation, and the single-element calculation are seen to increase with increasing strain. However, the differences between the strain (ε_{xx}, ε_{yy}, and γ_{xy}) distributions of the nonlocal and local 25-element calculations are very small compared to differences in the results for different specimen heights.

CONCLUSIONS

1. The previously formulated nonlocal microplane model for concrete is improved to describe the cyclic and rate-dependent behaviors. By contrast with the previous microplane model, the normal strain component on the microplane is not split into its volumetric and deviatoric parts; instead, the lateral normal strains are considered. The penalty is that the full range of Poisson's ratio cannot be covered, but the Poisson ratio values typical for concrete can be obtained. Furthermore, instead of one shear strain resultant on the microplane, the shear strain is represented by two shear components in the directions of two in-plane coordinates. This approach appears to eliminate some possibly unrealistic features of the calculated response on the microplanes (although this question cannot be decided by direct experimental observations).

2. The response of the normal strain component on the microplane is varied from hydrostatic response to plastic response and to softening response as a function of lateral normal strain on the same microplane. As before, the microplane strains are the resolved components of the macrostrain (kinematic constraint), but the response of the shear component is made to depend on the resolved normal component of the macroscopic stress tensor on the same microplane (which represents a static constraint). This allows it to represent more closely the physical concept of friction. The values of peak stress, strain at peak, ductility, and the postpeak shape of the descending stress-strain curve for the microplane components, can be used to control the macroscopic response in an easily understandable manner. In the case of monotonic loading tests, 10 microplane material parameters have to be identified by fitting test data.

3. To model rate dependence, a Maxwell-type rheologic model consisting of a linear viscous element with a constant relaxation time coupled in series with an elastoplastic-fracturing element is adopted for each microplane strain component. The exponential algorithm previously developed for creep (and previously also applied to a different microplane model) is adapted to this formulation to calculate the response for each microplane component in the time steps of numerical integration.

4. Nonlinear unloading-reloading hysteresis rules are developed for each elastoplastic-fracturing element using the concept of back-stress and objective-stress. Furthermore, cyclic rules are set up for the overall response of the generalized Maxwell model or each microplane component, covering both the tensile and compressive stress ranges and general strain histories.

5. The present microplane model describes reasonably well the existing test data from cyclic uniaxial compressive and tensile tests, triaxial compressive tests, and the strain-rate effect in uniaxial compressive tests. The model also realistically describes the strain-softening, damage processes, the hysteretic properties during unloading and reloading, the confinement effect on the transition from softening to hardening, and the hydrostatic response.

6. A nonlocal generalization of the present microplane model can well represent localization behavior and the effect of height-to-width ratio on uniaxial compressive softening. Generally, the numerical convergence of the finite-element calculations is not good for the local model, but is good for the nonlocal model.

ACKNOWLEDGMENT

The present results have been obtained under a joint research program between Shimizu Corporation, Tokyo, and Northwestern University. The first author wishes to thank Shimizu Corporation for giving him the opportunity to conduct this research at Northwestern University.

APPENDIX. REFERENCES

Bažant, Z. P., and Oh, B. H. (1983). "Crack band theory for fracture of concrete." *Matériaux et Constructions*, Paris, France, 16(93), 155–177.

Bažant, Z. P., and Oh, B. H. (1986). "Efficient numerical integration on the surface of a sphere." *Zeitschrift für Angewandte Mathematik und Mechanik*, Leipzig, Germany, 66(1), 37–49.

Bažant, Z. P., and Ožbolt, J. (1990). "Nonlocal microplane model for fracture, damage, and size effect in structures." *J. Engrg. Mech.*, ASCE, 116(11), 2485–2505.

Bažant, Z. P., and Prat, P. C. (1988a). "Microplane model for brittle-plastic material: I. Theory." *J. Engrg. Mech.*, ASCE, 114(10), 1672–1688.
Bažant, Z. P., and Prat, P. C. (1988b). "Microplane model for brittle-plastic material: II. Verification." *J. Engrg. Mech.*, ASCE, 114(10), 1689–1702.
Carol, I., Bažant, Z. P., and Prat, P. C. (1992). "New explicit microplane model or concrete: Theoretical aspects and numerical implementation." *Int. J. of Solids and Struct.*, 29(9), 1173–1191.
Dilger, W. H., Koch, R., and Kowalczyk, R. (1984). "Ductility of plain and confined concrete under different strain rates." *ACI J.*, 81(1), 73–81.
Green, S. J., and Swanson, S. R. (1973). "Static constitutive relations for concrete." *Rep. No. AFWL-TR-72-2*, Air Force Weapons Laboratory, Kirtland Air Force Base.
Hasegawa, T., and Bažant, Z. P. (1993). "Nonlocal Microplane concrete model with rate effect and load cycles. I: General formulation." *J. Mat. in Civ. Engrg.*, ASCE, 7(3), 372–393.
Karsan, D., and Jirsa, J. O. (1969). "Behavior of concrete under compressive loadings." *J. Struct. Div.*, ASCE, 95(12), 2543–2563.
Ožbolt, J., and Bažant, Z. P. (1991). "Cyclic microplane model for concrete." *Proc. Int. RILEM/ESIS Conf. on fracture processes in brittle disordered materials: concrete, rock, ceramics*, Chapman & Hall, London, England, 639–650.
Reinhardt, H. W., and Cornelissen, H. A. W. (1984). "Post-peak cyclic behaviour of concrete in uniaxial tensile and alternating tensile and compressive loading." *Cement and Concrete Res.*, 14(2), 263–270.
van Mier, J. G. M. (1984). "Strain-softening of concrete under multiaxial loading conditions," PhD thesis, Eindhoven University of Technology, Eindhoven, The Netherlands.
Willam, K., Hurlbut, B., and Sture, S. (1986). "Experimental and constitutive aspects of concrete failure." *Finite element analysis of reinforced concrete structures*, C. Meyer and H. Okamura, eds., ASCE, New York, N.Y., 226–254.